

# NUMERICAL SIMULATION OF ICE ACCRETION ON A PITOT TUBE

Krzysztof Szilder & Peter Forsyth

Aerospace Research Centre, National Research Council Canada

## Abstract

This paper presents numerical simulations of aircraft pitot/pitot-static tubes under supercooled liquid water icing conditions. Simulations are carried out with the probe mounted in a wind tunnel geometry, using icing conditions as defined by SAE AS5562 for the development and certification of pitot and pitot-static probes. The results presented include surface heat transfer distributions, droplet impingement distributions, and ice shapes, for glaze and rime icing conditions assuming no probe heating. A realistic variety of ice shapes are predicted, with notable changes in the shapes based on the icing conditions and probe orientation.

**Keywords:** ice accretion, numerical simulation, pitot probe

## 1. Introduction

Atmospheric icing occurs when airborne supercooled water droplets freeze on objects they encounter. This process is especially hazardous to aircraft when the ice build-up changes the lift-generation capability of aerodynamic surfaces and the stability and control characteristics of the aircraft as a whole. Undesirable ice can form on a variety of aircraft components including engine inlets, fuselage, windshield, antennae and probes. This paper focuses on pitot tubes, where even small amounts of accreted ice can have catastrophic consequences. The probes are at risk of performance degradation due to ice accretion that can block the stagnation ports or runback water that can flow into static ports, thus providing incorrect airspeed readings to the pilot that can lead to fatal accidents, e.g., Air France flight 447 [1] in 2009.

To mitigate icing events, pitot tubes have anti-icing systems comprised of embedded electrical heaters. The probe anti-icing system goes through a rigorous design and certification process, using full-scale wind tunnel testing at simulated atmospheric conditions, as defined by international standards such as SAE AS5562 [2]. This process usually requires a number of wind-tunnel entries to determine the best distribution of the available heating power density inside the probe, within the limits of the total power available as set by the airframer. At certification, the probe must be demonstrated to remain fully functional under a wide range of atmospheric conditions. The ability to correctly simulate how ice accretes and how tube heating influences ice formation is essential in developing mitigation strategies, and can help shorten the research and development cycles before the designer can certify their probe for flight.

## 2. Model Description and Numerical Set-up

### 2.1 Geometry and Mesh Generation

The probe geometry is generic and indicative of typical aircraft pitot/pitot-static probes tested at the NRC Altitude Icing Wind Tunnel (AIWT) facility, as shown in Figure 1. The probe barrel has a 250 mm length and a 9 mm radius. The probe tip is a conical frustum with a minor radius of 4 mm and a major radius of 9 mm, and has a length of 13.7 mm (expansion angle  $75^\circ$ ) included in the above-barrel length. The probe arm/strut has a length of 120.4 mm, with an elliptical cross section (semi-major axis

of 40 mm, semi-minor axis of 9 mm), and is swept aft of the probe barrel axis at  $34^\circ$  making the centreline of the barrel 100 mm above the arm root/splitter plate. The probe is mounted on a 356 mm  $\times$  176 mm  $\times$  2.5 mm thick splitter plate, as per AS5562. The splitter plate is mounted on a 40 mm radius column that is 80 mm in length; this splitter plate – column assembly is the ‘mount’. In turn, the probe – mount assembly is mounted in a geometry indicative of the AIWT high speed insert (520 mm  $\times$  330 mm cross section as per the wind tunnel, axial length extended to 2000 mm for numerical stability). The probe is mounted on a vertical side wall as in experiments, but the geometry is shown throughout this paper rotated  $90^\circ$  about the x-axis.

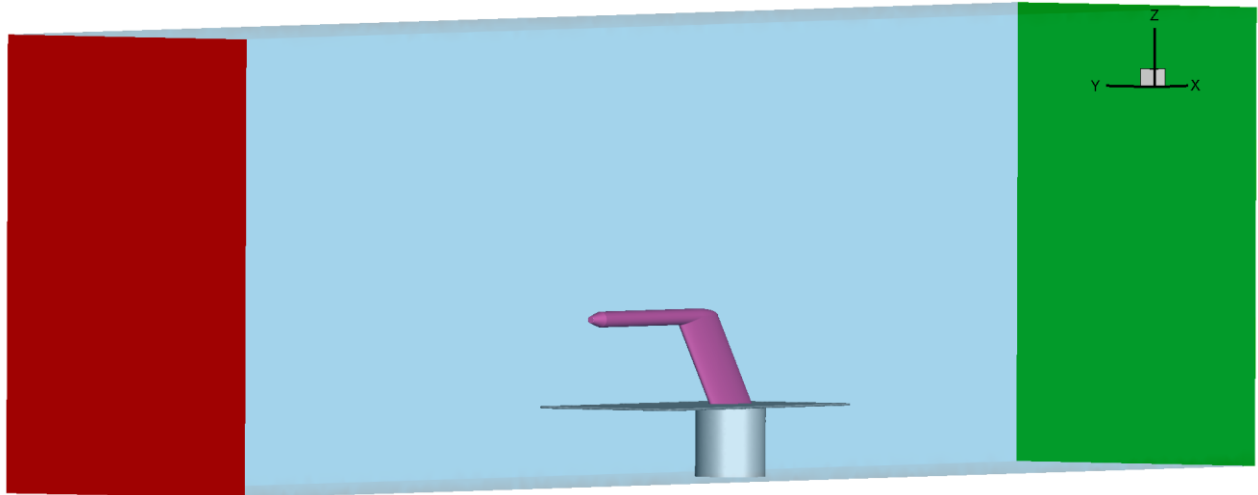


Figure 1. Simulation domain. Left to right: inlet (red), test section (blue, transparent), probe (fuchsia), splitter plate and mount (grey), outlet (green). The y-axis and z-axis are orientated in the horizontal directions, and the y-axis in the vertical, with gravity acting in the negative y-direction. Probe is shown at  $0^\circ$  AoA, with a positive angle of attack (AoA) towards the starboard wall of the tunnel, as-viewed.

The probe tip is kept on the centreline of the tunnel in the narrow dimension. For the  $15^\circ$  AoA cases this means moving the mount and probe towards the port wall, and rotating the probe to starboard; the splitter plate and mount are not rotated. This matches the experimental approach used for the assessment of probes in the AIWT.

The tip of a physical pitot probe is open for the measurement of total pressure. In this work, a closed tip geometry was used, which occurs when ice accretion causes the probe tip to plug during the initial stages of de-icing tests. This is later referred to as the ‘tip face’. See section 2.2 for further details.

Mesh generation for CFD computations was carried out using ANSYS ICEM CFD [3]. Unstructured tetrahedral meshes were generated with a cell size of 0.5 mm on the probe tip and 1 mm on the probe barrel and arm. A 2 mm cell size was used on the splitter plate and mount. Prism inflation layers were grown to resolve the boundary layer, giving a non-dimensional wall distance  $y^+ < 1$  across all probe and mount surfaces (first cell height of 5  $\mu\text{m}$ , expansion ratio of 1.3, 20 layers total, and total prism thickness of 3.1 mm).

## 2.2 Case Descriptions and Conditions

Four cases were run from AS5562: L1 (lower altitude, lower speed) and L2 (higher altitude, higher speed) at  $0^\circ$  and  $15^\circ$  AoA. Class 3 & 4 aircraft (‘jet transport’ and ‘business jet’) were considered, with the conditions given in Table 1. Probe manufacturers usually provide a multiplicative concentration factor for liquid water content (LWC) to account for increase of concentration of droplets around the aircraft body, and this value tends to be in the region of 1.0 to 2.0. Concentration factors are not considered in this work for simplicity. The Reynolds number is calculated based on the freestream conditions and barrel diameter.

No probe heating is applied and hence no probe anti-icing is simulated. Initially the probe surface temperature is set equal to the freestream static temperature, and the ice accretion is allowed to

grow. This is representative of the first stage of the AS5562 de-icing tests, and allows the model to be assessed without the added complexity of significant water runback resulting from anti-icing heating.

Test condition	Altitude (kft)	Mach number, Ma	Static air temperature, T (°C)	Velocity, V (m/s)	Reynolds number, Re	MVD (µm)	LWC (g/m <sup>3</sup> )	Angle of attack, AoA (°)
L1	5	0.40	-10	130	157 000	20	0.6	0 & 15
L2	10	0.56	-20	179	191 000	20	0.3	0 & 15

Table 1. Simulation conditions, as per AS5562 for class 3 & 4 aircraft.

### 2.3 Flow Simulation

The flow solution was carried out using Cobalt [4], a finite-volume unstructured Navier-Stokes solver. Steady Reynolds-averaged Navier-Stokes computations were undertaken using the Spalart-Allmaras turbulence model [5]. Second-order spatial accuracy was applied by second-order Taylor series expansion in-cell; second-order gradients were computed through the least-squares method. A mass flow rate boundary condition was used at the inlet, and a fixed static pressure, based on pressure altitude, was used at the outlet. Non-slip, wall boundary conditions were used, isothermal (0°C) on the probe and adiabatic on the mount and test section walls.

### 2.4 Droplet Trajectory and Impingement Distribution

Droplet trajectories were calculated using an in-house MATLAB-based code. Lagrangian particle tracking was utilized, with a force balance considering spherical drag and gravity. Droplet velocities and positions were computed via trapezoidal integration. A single droplet size equal to a median volumetric diameter (MVD) of 20 µm was used, with a droplet density of 1 000 kg/m<sup>3</sup>.

The droplet collision efficiency distribution,  $\beta$ , was generated by considering the change in cross-sectional area of an initially-square streamtube of a droplet from injection to impact,

$$\beta = \frac{A_0}{A_1} \tag{1}$$

Here  $A_0$  is the initial streamtube cross sectional area at droplet injection and  $A_1$  is the streamtube cross sectional area at impact. Droplets were injected in a grid with 0.5 mm spacing, 0.5 m upstream of the probe tip, with their initial velocity interpolated to that of the local freestream velocity. As the wetted/windward area of the probe increases with increasing angle of attack, this corresponds to approximately 9 100 droplets for the 0° AoA cases and 38 200 droplets for the 15° AoA cases. Adaptive time stepping was used: 25 µs far from the probe surfaces, reduced to 12.5 µs in the vicinity of the probe (droplet-wall distance of less than 10 mm). A ‘nearest neighbour’ method is used to interpolate the beta distribution to the CFD grid locations, with a maximum interpolation distance of 2 mm allowed between grid points and droplet impact locations. Beyond this distance, zero impingement is considered to occur.

### 2.5 Morphogenetic Model

The morphogenetic model predicts ice accretion using the results from the CFD and droplet trajectory calculations. The “morphogenetic” approach, a unique icing modelling capability developed at the NRC, is based on a discrete fluid element formulation and simulation of ice formation physics. This methodology has been successfully used to predict ice accretion on a variety of engineering structures from aircraft wings [6] [7] to bridge cables [8]. This innovative approach has many advantages over traditional simulation methods. Whereas traditional icing models consider

continuous fluxes of impinging airborne liquid and the resulting water flow along the surfaces, the morphogenetic approach considers the behaviour of individual fluid elements, which impinge, move along the icing surface, and freeze according to physically-based stochastic rules. In the morphogenetic ice accretion model, the mass flux of impinging droplets is divided into fluid elements that typically represent a small ensemble of individual cloud drops. A three-dimensional, rectangular, cubic lattice defines the accretion domain. By building the accretion one element at a time on this lattice, the morphogenetic model emulates the time evolution of the accretion shape, in a way that mimics the real world. In this model, the fluid elements are allowed to impact randomly on the surface or on the existing ice structure in such a way that their mass distribution is consistent with the overall droplet impact distribution. The model is also capable of an analysis of the consequences of a thermal anti-icing system on the ice accretion process and the resulting runback ice formation [7]. An anti-icing heating module has been implemented by adding additional heat flux to the ice accretion energy equation. This equation is solved to determine the rate of ice growth, amount of water runback, and evaporative mass flux.

A single time step approach is taken in this work, where ice accretion is calculated from the clean surface distributions. This has been shown to reproduce experimental ice shapes on aerofoil geometries acceptably [9], but accurate solution of large glaze shapes can require multiple re-meshing and re-resolution sub-steps.

### 3. Results

#### 3.1 Surface Distributions

##### 3.1.1 Heat Transfer

The convective heat transfer from surfaces where ice accretion forms is a crucial parameter for the correct prediction of glaze ice shapes. Consequently, special attention is paid to this parameter. The heat transfer distributions throughout this work are based on the clean (ice-free) surface geometry. Convective heat transfer distributions are reported in Figure 2 as Frössling number,

$$Fr = \frac{Nu}{\sqrt{Re}} \quad (2)$$

where  $Nu$  is Nusselt number  $Nu = hd/k$ , where  $h$  is the convective heat transfer coefficient,  $d$  is the characteristic length (barrel diameter), and  $k$  is the air thermal conductivity, and  $Re$  is the Reynolds number based on freestream conditions and barrel diameter. The same viewing position and angle is used for both angles of attack; hence, the  $15^\circ$  AoA plots show the windward side of the arm, Figures 2 and 3. The windward side is of interest since this is where drops tend to impinge and ice is formed.

When reduced to Frössling number, the main independent variable becomes the angle of attack for heat transfer under a set of given conditions. For the L1/  $0^\circ$  AoA and L2/  $0^\circ$  AoA cases, Figure 2 a, c, the tip distributions are close to identical, with a small region of low heat transfer just aft of the tip face where a flow separation is observed. Small asymmetries are observed between the freestream and splitter plane sides of the tip, upper and lower respectively as viewed, likely due to the presence of the splitter plate. Aft of the conical section of the tip, low heat transfer is observed on the barrel, with case L1/  $0^\circ$  AoA showing slightly lower heat transfer in this region than case L2/  $0^\circ$  AoA. Moving aft, high heat transfer and the highest values of Frössling number are found at the arm-barrel junction, where flow washes up the junction line, and a horseshoe vortex is generated. A region of high heat transfer is also observed on the arm leading edge just outboard of the root, again due to a horseshoe vortex.

The L1/  $15^\circ$  AoA and L2/  $15^\circ$  AoA cases, Figure 2 b, d, indicate more uniform heat transfer across the windward faces of the probe tip than the  $0^\circ$  AoA cases. The separation behind the tip face does not occur as strongly, though separation does occur as the conical tip transitions to the barrel. Heat transfer is higher on the barrel for both  $15^\circ$  AoA cases than the  $0^\circ$  AoA cases, but is lower on the arm. The flow at the barrel-arm junction now sweeps over the windward face, towards the freestream side of the barrel, rather than along the junction line.

At both the L1/ 0° AoA and L2/ 0° AoA conditions, changing to 15° AoA results in an increase of 4.5% in the integral convective heat transfer. At L1/ 0° AoA, changing to the L2/ 0° AoA condition results in an increase of 24% in the integral convective heat transfer.

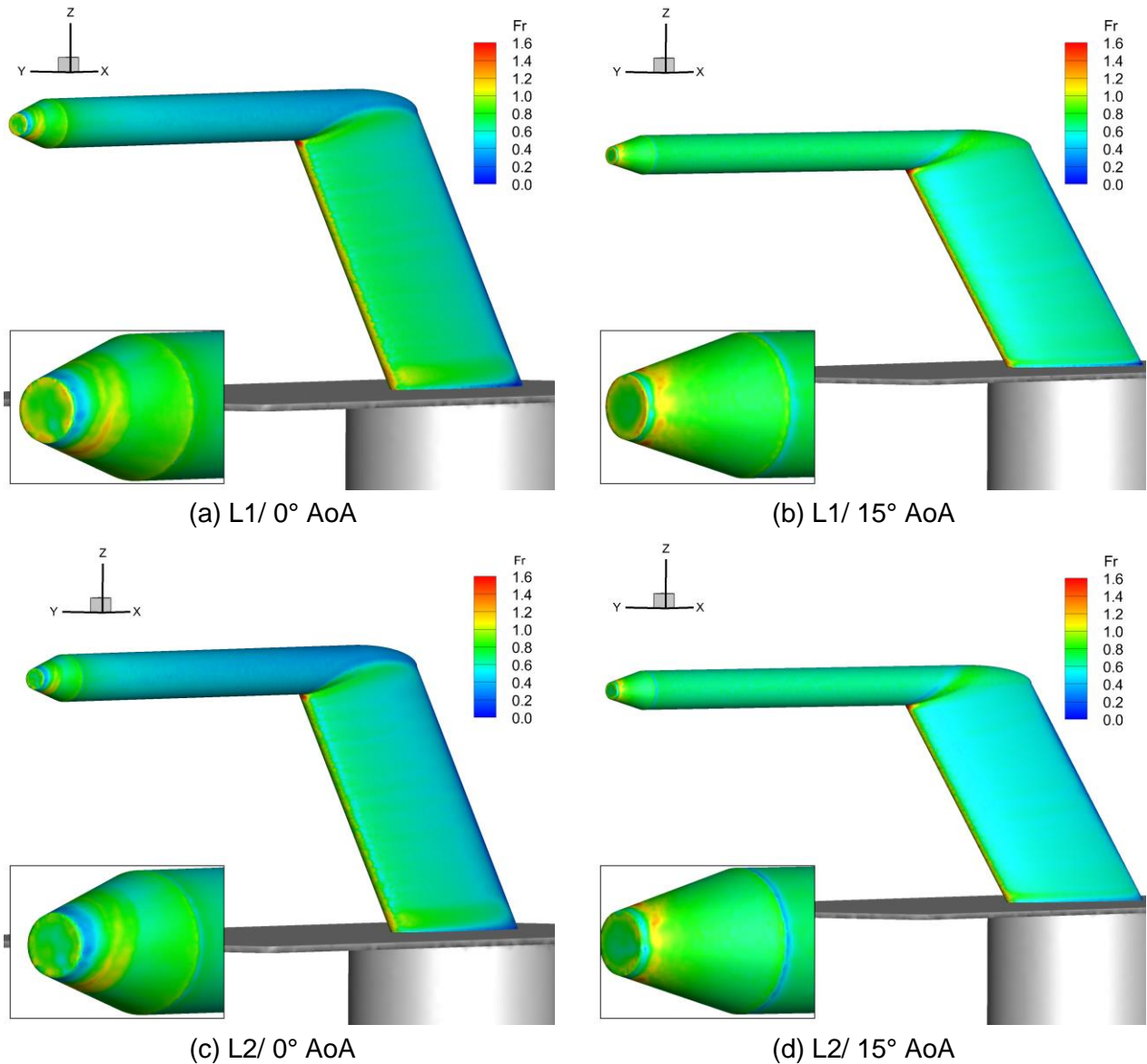


Figure 2. Frössling number distributions. Same viewing angle throughout.

### 3.1.2 Droplet Impingement

Collision efficiency distributions,  $\beta$ , for each test case are shown in Figure 3. The main variable affecting the global  $\beta$  distribution is again the angle of attack: at 0° AoA, Figure 3 a, c, impingement mainly occurs on the front face of the probe tip and the leading edge of the arm. On the conical tip,  $\beta$  values are uniform, and increase with increasing freestream speed ( $V_{L2} > V_{L1}$ , see Table 1) but no impingement occurs on the barrel at 0° AoA. A small region of high density droplet impact,  $\beta > 1$ , occurs on the arm leading edge, close to the barrel. Here, droplets that were driven towards the splitter plate by the presence of the probe tip are concentrated by the flow moving along the arm-barrel junction. This has the effect of causing a localized region of high impingement. The slight discontinuities in the profile in this region are due to the achievable droplet resolution at injection. On the arm leading edge,  $\beta$  values are extremely similar between the two cases, with values of  $\beta = 0.79$  (L1/ 0° AoA) and  $\beta = 0.80$  (L2/ 0° AoA). This similarity is reflected in the results of the analytical

solution of Langmuir and Blodgett for impingement on a cylinder [10]. This analytical solution uses a 'modified inertia parameter', calculated from the droplet Stokes number and modified by a dimensionless range parameter, which relates the actual droplet drag to that given by Stokes (i.e., low Reynolds) drag. A detailed description is given in [11]. Using an inscribed leading-edge radius of 2 mm, the analytical solution gives  $\beta = 0.76$  (L1/ 0° AoA) and  $\beta = 0.78$  (L2/ 0° AoA), accounting for the sweep of the arm. Both cases show a shadow zone around the arm root, caused by the splitter plate leading edge. Outboard of (above) the shadow zone, a local high impingement spot is formed, as the shadow zone droplets are driven outboard.

For cases L1/ 15° AoA and L2/ 15° AoA, Figure 3 b, d, impingement on the tip face is lower than for the 0° AoA but up to twice as high on the windward face of the conical tip. Collision efficiency levels are increased on the windward face of the barrel. Comparisons at the stagnation line along the barrel to the analytical solution are extremely close: for case L1/ 15° AoA,  $\beta = 0.21$  for the simulation and  $\beta = 0.20$  analytically. Note here that the barrel diameter (18 mm) and sweep angle (75° at 15° AoA) are used. For case L2/ 15° AoA,  $\beta = 0.22$  for the simulation and  $\beta = 0.21$  analytically. No region of high impingement is seen at the outboard end of the arm, close to the barrel, for the 15° AoA cases as was seen for the 0° AoA cases. On the arm, leading edge  $\beta$  values are very similar to 0° AoA, but the chordwise extent of the impingement is 2.3 times greater than at 0° AoA.

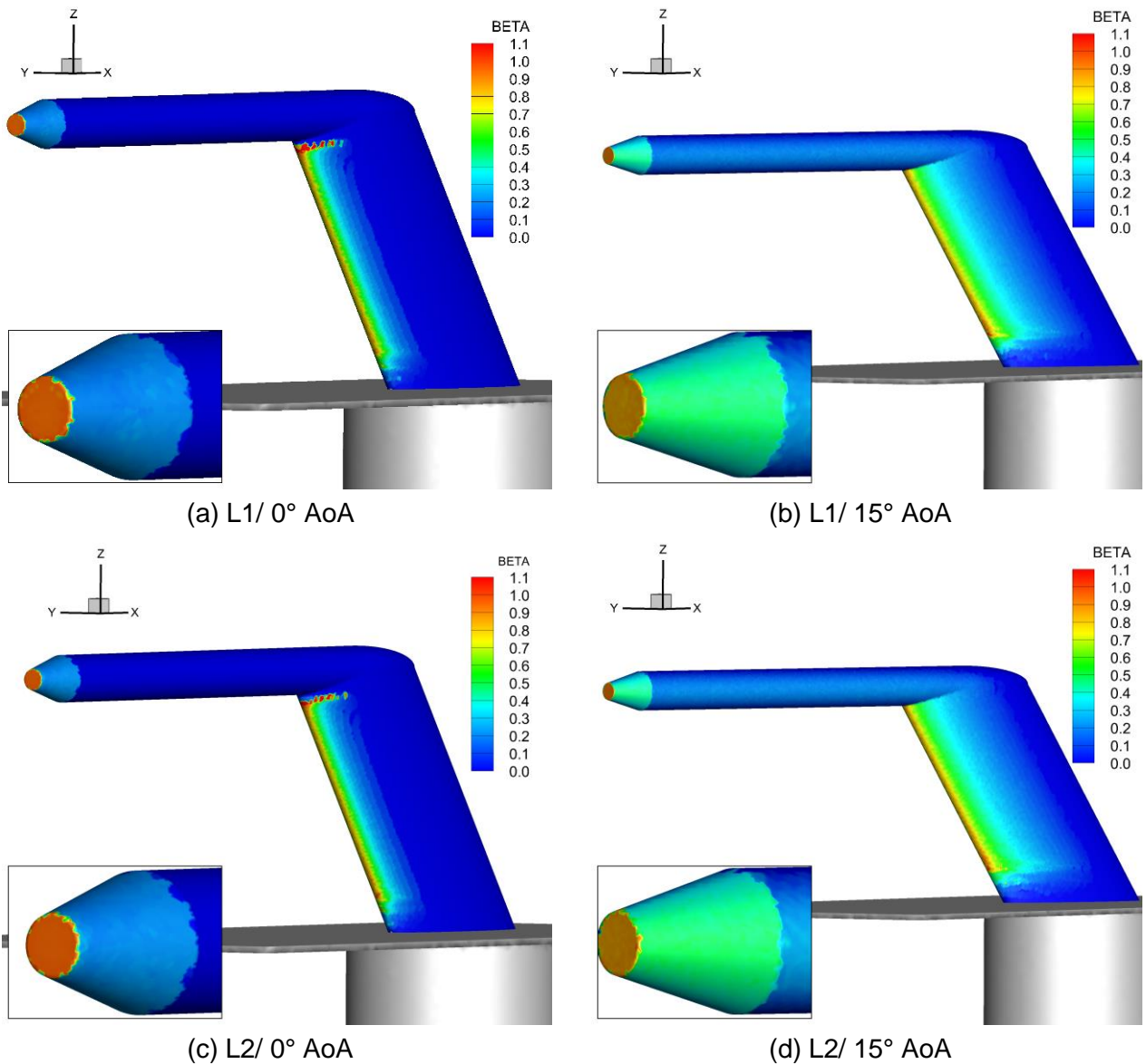


Figure 3. Collision efficiency,  $\beta$ , distributions.

### 3.2 Ice Accretion

Ice accretion was computed using the morphogenetic approach on two regions of the probe: the tip vicinity and a 1 cm wide section at midspan on the arm. All ice accretion simulations were run for 1 minute.

#### 3.2.1 Cases L1/ 0° AoA and L2/ 0° AoA

For the L1 conditions and 0° AoA, the tip ice accretion, Figure 4 a, shows the characteristic horn shape of glaze icing due to impinging water not freezing at impact and running back before freezing downstream. While the ice initially forms across the whole tip (tip face and conical section), the face accretion grows large enough to form a shadow zone behind it that stops further accretion on the aft portion of the tip cone; this is very evident in the upper image of Figure 4 a. Ice accretion on the arm, Figure 4 b, tends to be glaze ice with comparatively uniform thickness. The accretion is observed to be fairly smooth relative to the rime ice accretion of case L2/ 0° AoA, which is another indication of runback occurring.

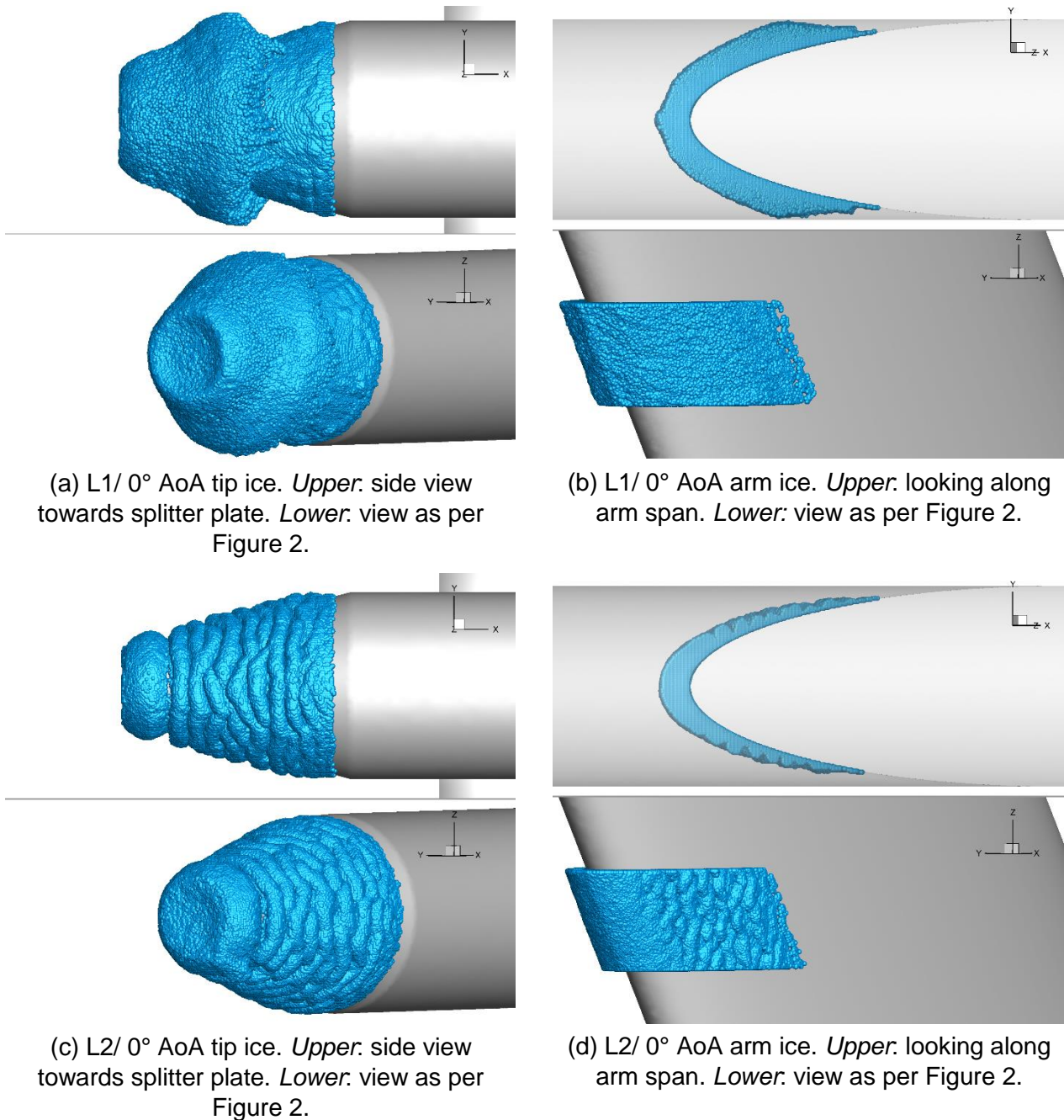


Figure 4: Ice shapes for cases of 0° angle of attack.

In comparison, the L2/ 0° AoA accretion shows more pronounced mixed rime-glaze ice accretion, Figure 4 c. A small glaze ice region exists on the tip face, where the impinging water mass is at a maximum, changing to rime ice further downstream on the conical section as the freezing fraction increases to unity. The rime ice region is characterized by rough surface features. Similar processes occur on the arm, Figure 4 d, resulting in a glaze ice region followed by a rime ice region moving downstream. As the aft portion of the L2/ 0° AoA accretion on the arm is fully rime ice, no runback is occurring and the chordwise length of the accretion is shorter than for L1/ 0° AoA. From comparison of the arm accretion cross-sections (upper plots, Figure 4 b, d), the difference between the glaze ice and rime ice formations is clearly visible. For L2/ 0° AoA, the ice accretion decreases in thickness downstream of the leading edge, as almost all impinging water freezes on contact, and  $\beta$  decreases aft of the leading edge. In comparison, for case L1/ 0° AoA, the ice accretion thickens downstream of the leading edge, indicating substantial runback. The chordwise extent of the L1/ 0° AoA ice is 7% greater than for L2/ 0° AoA, due to the runback water freezing and forming glaze ice downstream of the impingement limits.

For the 0° AoA cases, the ice accreting on the probe tip and probe arm forms symmetrically. As a result of higher LWC for L1 conditions, and in spite of lower velocity, the total ice accretion mass is greater for the L1 case. In addition, the warmer air temperature and lower air speed of the L1 case increases the size of the glaze ice region.

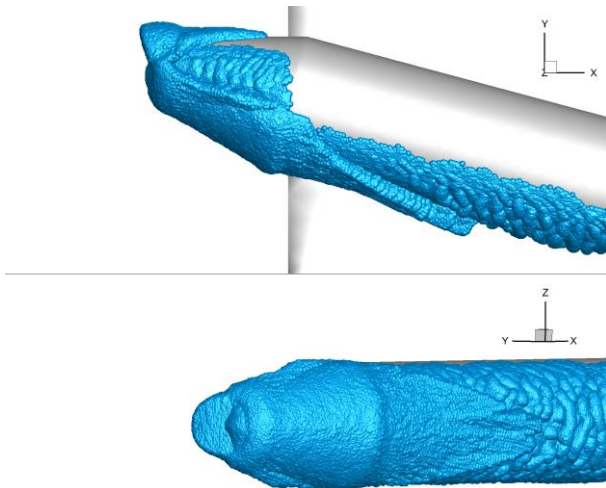
### 3.2.2 Cases L1/ 15° AoA and L2/ 15° AoA

When the pitot tube is mounted at 15° AoA, Figure 5, the ice forms in a non-symmetrical manner. Droplet impingement occurs on the windward face of the probe and complex 3D glaze and rime ice features result from the interactions between droplet impingement, surface water flow and convective heat transfer distributions.

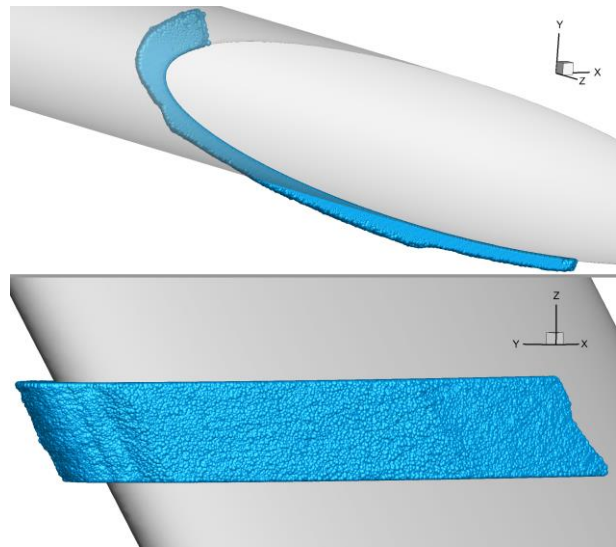
For the L1 conditions, Figure 5 a, glaze ice forms on the windward probe tip that is exposed to a high rate of droplet impingement. Aft of the tip, unfrozen water continues to flow downstream on the barrel, forming pronounced ice features. This ice growth is enhanced by the collection of droplets that initially impinge on barrel locations further downstream. Aft on the barrel, rime ice is formed. On the probe leeward side, the ice growth is substantially smaller and formed only from runback water, as no droplet impingement occurs in this region (shape visible in the upper image of Figure 5 a). In addition, lower impingement intensity on the sides of the probe tip leads to rime ice formation (same image).

Ice formation on the arm is non-symmetrical and predominantly forms as glaze ice, Figure 5 b. The glaze ice forming on the windward face has relatively uniform thickness, as runback water flow compensates for reduced water impingement at the more downstream locations. On the leeward side of the arm, where droplet impingement does not occur, enhanced heat transfer and substantial runback water flow from the leading edge leads to a small region of greater ice thickness, upper image of Figure 5 b. The greater chordwise extent of the ice at 15° AoA relative to 0° AoA can be seen in comparison with Figure 4 b, noting that the spanwise extent of the ice shown is equal (1 cm).

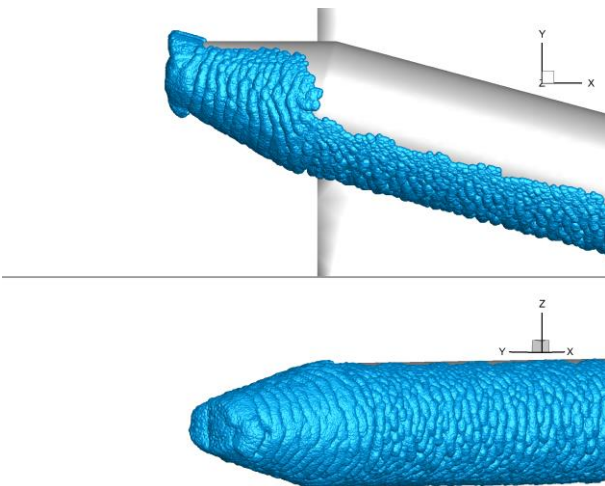
Under L2 conditions, rime ice mostly forms with its characteristic rough surface, as a result of the lower LWC and colder air temperature. Rime ice covers the area of droplet impingement and its thickness is closely related to the droplet impingement distribution. Only at locations of maximum intensity of droplet impingement at the tip, Figure 5 c, and the arm leading edge, Figure 5d, glaze forms due to insufficient heat transfer to freeze all impinging drops on impact. Another interesting feature is that as the stagnation line moves further aft on the windward surface for case L2/ 15° AoA, relative to its position for L1/ 15° AoA, and the size of the ice 'hook' onto the leeward face decreases as more of the runback water flows onto the windward face (compare upper images of Figure 5 b and d). The chordwise extent of the L1/ 15° AoA arm (glaze) ice is 13% larger than for the L2/ 15° arm AoA (rime) ice, again due to runback beyond the impingement limit for case L1/ 15° AoA.



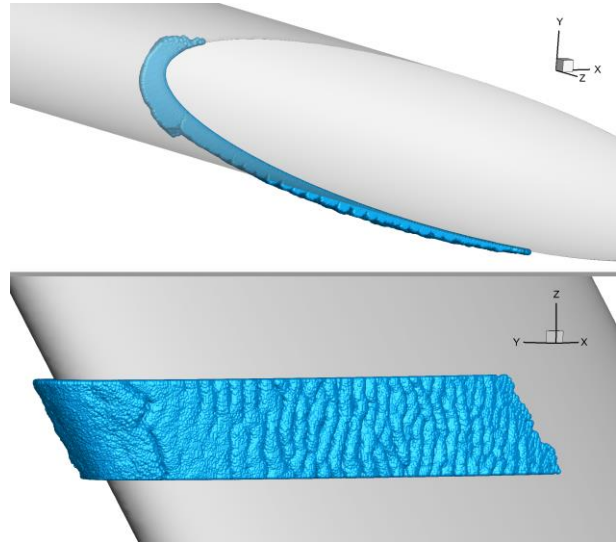
(a) L1/ 15° AoA tip and barrel ice. *Upper:* view from above towards splitter plate. *Lower:* windward view, as per Figure 2.



(b) L1/ 15° AoA arm ice. *Upper:* looking along arm span. *Lower:* windward face.



(c) L2/ 15° AoA tip and barrel ice. *Upper:* view from above towards splitter plate. *Lower:* windward view, as per Figure 2.



(d) L2/ 15° AoA arm ice. *Upper:* looking along arm span. *Lower:* windward face.

Figure 5. Ice shapes for cases of 15° angle of attack.

#### 4. Conclusions

A set of numerical tools has been developed that is capable of predicting ice formation on a pitot tube placed in an icing wind tunnel. The CFD module predicts airflow and surface heat transfer, the results of which are used by an in-house droplet trajectory module to predict the droplet impingement distribution. The morphogenetic code computes the ice shape, based on the surface distributions from the preceding calculations. The results show realistic shapes, including rime and glaze ice regions, for different icing conditions and pitot tube orientations.

This paper has presented initial simulation results. The next step is to extend the simulations to include anti-icing heating of the pitot probe. Experimental work will also be completed to validate the numerical results for both heat transfer and ice accretion shapes in the NRC's Altitude Icing Wind Tunnel.

## Contact Author Email Addresses

Any correspondence should be made using the following addresses:

Krzysztof Szilder: [Krzysztof.Szilder@nrc-cnrc.gc.ca](mailto:Krzysztof.Szilder@nrc-cnrc.gc.ca)

Peter Forsyth: [Peter.Forsyth@nrc-cnrc.gc.ca](mailto:Peter.Forsyth@nrc-cnrc.gc.ca)

## Copyright Statement

The authors confirm that they, and/or their company or organization, hold copyright on all of the original material included in this paper. The authors also confirm that they have obtained permission, from the copyright holder of any third party material included in this paper, to publish it as part of their paper. The authors confirm that they give permission, or have obtained permission from the copyright holder of this paper, for the publication and distribution of this paper as part of the ICAS proceedings or as individual off-prints from the proceedings.

## References

- [1] Bureau d'Enquêtes et d'Analyses, "On the accident on 1st June 2009 to the Airbus A330-203 registered F-GZCP operated by Air France flight AF 447 Rio de Janeiro - Paris," 2012.
- [2] SAE, *Ice and Rain Minimum Qualification Standards for Pitot and Pitot-static Probes, AS5562*, 2020.
- [3] Ansys Inc., *ANSYS ICEM CFD theory guide*, 2021.
- [4] W. Z. Strang, R. F. Tomaro and M. J. Grismer, "The defining methods of Cobalt60: a parallel, implicit, unstructured Euler/Navier-Stokes flow solver," in *37th AIAA Aerospace Sciences Meeting and Exhibit*, 1999.
- [5] P. R. Spalart and S. R. Allmaras, "A One-Equation Turbulence Model for Aerodynamic Flows," *La Recherche Aérospatiale*, vol. 1, pp. 5-21, 1994.
- [6] K. Szilder and E. P. Lozowski, "Novel two-dimensional modeling approach for aircraft icing," *J. Aircr.*, vol. 41, no. 4, p. 854–861, 2004.
- [7] K. Szilder and E. Lozowski, "Numerical simulation of ice accretion influenced by anti-icing heating system," in *ICAS 2018*, 2018.
- [8] K. Szilder, A. D'Auteuil and S. McTavish, "Predicting ice accretion from freezing rain on bridge stay cables," *Cold Reg. Sci. Technol.*, vol. 187, p. 103285, 2021.
- [9] P. Forsyth and K. Szilder, "Application of the Morphogenetic Approach to 1st AIAA Ice Prediction Workshop Test Cases," in *AIAA Aviation Forum*, Chicago, 2022.
- [10] I. Langmuir and K. Blodgett, "A Mathematical Investigation of Water Droplet Trajectories," Army Air Forces Technical Report No. 5418, 1946.
- [11] D. Anderson, "Manual of Scaling Methods, NASA/CR—2004-212875," NASA, 2004.